A 0.038-mm^2 SAW-Less Multiband Transceiver Using an N-Path SC Gain Loop

Gengzhen Qi, *Student Member, IEEE*, Pui-In Mak, *Senior Member, IEEE*, and Rui P. Martins, *Fellow, IEEE*

***Abstract*— An N-path switched-capacitor (SC) gain loop is proposed as an area-efficient surface acoustic wave-less wireless transceiver (TXR) for multiband TDD communications. Unlike the direct-conversion transmitter (TX: baseband (BB) filter → I/Q modulation → PA driver) and receiver (RX: LNA → I/Q demodulation → BB Filter) that the functions are arranged in an open-loop style, here the signal amplification, bandpass filtering, and I/Q (de)modulation are unified in a closed-loop formation, being reconfigurable as a TX or RX with a local oscillator (LO)-defined center frequency. The key advantages are the multiband operation capability in the TX mode, and high resilience to out-of-band (OB) blockers in the RX mode. Fabricated in a 65-nm CMOS, the TXR prototype consumes up to 38.4 mW (20 mW) in the TX (RX) mode at the 1.88-GHz long-term evolution (LTE)-band2. The LO-defined center frequency covers >80% of the TDD-LTE bands with neither on-chip inductors nor external input-matching components. By properly injecting (extracting) the signals into (from) the N-path SC gain loop, the TX mode achieves an −1 dBm output power, a −40 dBc $\text{ACLR}_{\text{EUTRA1}}$, and a 2% EVM at 1.88 GHz, while showing a −154.5 dBc/Hz OB noise at 80-MHz offset. In the RX mode, a 3.2-dB noise figure and a +8 dBm OB-IIP3 are measured. The active area (0.038 mm^2) of the TXR is 24× smaller than the state-of-the-art LTE solutions.**

***Index Terms*— Adjacent-channel leakage rejection (ACLR), bandpass filter, baseband (BB), blocker, CMOS, long-term evolution (LTE), Miller effect, multiband, N path, noise figure (NF), out of band (OB), passive mixer, phase noise, power-amplifier driver (PAD), receiver (RX), surface acoustic wave (SAW), switched capacitor (SC), transceiver (TXR), transmitter (TX).**

I. Introduction

IN ORDER to develop multiband cellular radios at low-cost, on-chip N-path switched-capacitor (SC) filters [1] are rekindled as a promising replacement of the off-chip surface acoustic wave (SAW) filters. The improved speed and parasitic effects of ultra-scaled CMOS technologies enable the N-path SC filters to provide tunable high-Q filtering over a wide range of frequencies [2], [3]. Beyond filtering, N-path mixing also facilitates wideband receivers (RXs) to achieve input matching and harmonic rejection [4]–[6]. The mixer-first wideband RX [4] shows a high out-of-band (OB)-IIP3 (+25 dBm) while covering a wide RF range (0.1–2.4 GHz), but the noise figure (NF) (5 dB) becomes a hard tradeoff with the power consumption (70 mW) due to the absence of RF gain. The noise-canceling RX [5] balances better between the OB-IIP3 (+13.5 dBm) and NF (1.9 dB), but its dual-path topology involves extra mixing and baseband (BB) circuitries, consuming more area (1.2 mm^2) and power (78 mW). Recently, the *gain-boosted* N-path technique was reported. It leads to a single-mixing blocker-tolerant RX [6] with competitive OB-IIP3 (+13 dBm) and NF (1.5–2.9 dB) at smaller area (0.028 mm^2) and power (11 mW). Regrettably, it demands a high gain-boosting factor (200 mS), which strongly restricts the signal bandwidth (BW = 2.6 MHz) and RF coverage (<1.5 GHz); both are inadequate for modern cellular standards such as the LTE.

SAW-less transmitters (TXs) confront a different challenge as the effort is on lowering the OB noise and spectral leakage, especially at the nearby RX bands (<100-MHz offset). The SAW-less TX in [7] exploits direct-quadrature voltage modulation to lower the OB noise (−159 dBc/Hz at 40-MHz offset) and raise the power efficiency (5.7%). Its power-amplifier driver (PAD) is the only gain stage, rendering the OB noise primarily dominated by the thermal noise of the passive mixers, and phase noise of the local oscillator (LO) generator. Nevertheless, its PAD relies on a passive *LC* load to deliver the required output power (P_{out}) and suppress the OB harmonics, being inflexible to support multiband communications. In fact, recent SAW-less multiband TXs still rely on dedicated baluns to extend the RF coverage. An example is the current-mode SAW-less TX in [8] that exhibits a −158 dBc/Hz OB noise at the RX band (30-MHz offset), but demands large die area (1.06 mm^2), and power (96 mW) for its mixer and voltage-to-current converter that have to be linear and low noise.

This paper proposes an *N-Path SC Gain Loop* as a SAW-less TXR for multiband TDD communications, entailing no on-chip inductors or external passives for input matching. Unlike the typical TXRs where the building blocks are cascaded in an open-loop style to build up the RF-to-BB (or BB-to-RF) signal-processing chain, here our N-path SC gain loop operates in a closed-loop style to unify the TX and RX functions, making possible of a very compact multiband TXR (0.038 mm^2). Measured at the LTE-band2 (1.88 GHz) and band5 (0.836 GHz), the TX mode exhibits an $\text{ACLR}_{\text{EUTRA1}} <$ −40 dBc, an EVM ≤ 2.1% and a low output noise of

Manuscript received December 28, 2016; revised March 22, 2017; accepted April 18, 2017. Date of publication May 18, 2017; date of current version July 20, 2017. This work was supported in part by the Macao Science and Technology Development Fund, in part by SKL Fund, and in part by the University of Macau Multi-Year Research Fund (MYRG2015-00040-FST). This paper was approved by Associate Editor Pietro Andreani. *(Corresponding author: Pui-In Mak)*

G. Qi and P.-I. Mak are with the State-Key Laboratory of Analog and Mixed-Signal VLSI and FST-ECE, University of Macau, Macau 999078, China (e-mail: pimak@umac.mo).

R. P. Martins is with the State-Key Laboratory of Analog and Mixed-Signal VLSI and FST-ECE, University of Macau, Macau 999078, China, on leave from the Instituto Superior Técnico, Universidade de Lisboa, 1049-001 Lisbon, Portugal.

Color versions of one or more of the figures in this paper are available online at http://ieeexplore.ieee.org.

Digital Object Identifier 10.1109/JSSC.2017.2697409

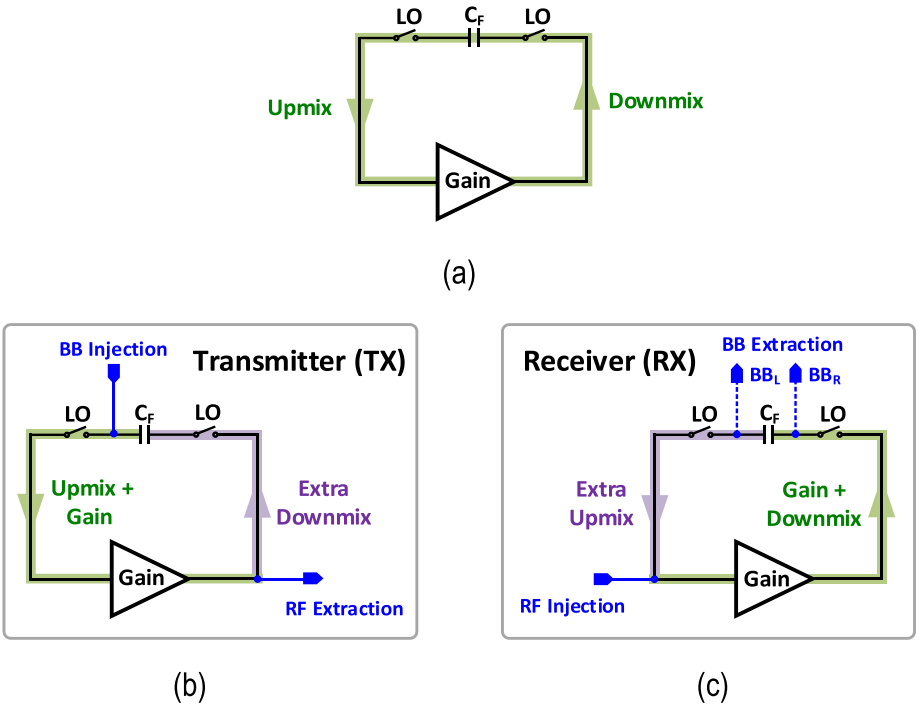

Fig. 1. (a) *SC gain Loop* performs gain, downmix, and upmix in a self-feed manner. It can operate as a (b) TX under BB-injection RF-extraction or (c) RX under RF-injection BB extraction. The extra downmix and upmix paths allow gain-boosted N-path filtering. For RX, there are two BB-extraction solutions BB_L (without right-hand switch) and BB_R.

<-154 dBc/Hz at 80-MHz offset. The RX mode draws 20-mW power, and exhibits a 3.2-dB NF and a +8-dBm OB-IIP3 at 1.88 GHz.

This paper is organized as follows: Section II introduces the properties of the SC gain loop that holds a number of promises of being a reconfigurable TXR. Section III describes how the gain-boosted N-path technique can be embedded into the SC gain loop to build the SAW-less TX mode [9]. In Section IV, the SAW-less RX mode utilizing a switched-BB-extraction technique is reported as a follow-up work of [10] and [11] to improve further the NF. Note that the theory and modeling of the gain-boosted N-path LNA and receiver have been established in [10] and [11], and will not be covered here. Section V describes the LO generator with the TX/RX-mode control logics, followed by the measurement results in Section VI. The conclusions are drawn in Section VII.

II. Principle of the SC Gain Loop as a TXR

Comparatively, an SAW-less RX should be able to amplify a weak in-band (IB) signal in the presence of large OB blockers, whereas an SAW-less TX should be able to deliver a large IB signal with low OB noise and spectral leakages. Such discrepancy inspires the exploration of a *RX–TX-compatible N-path technique* to implement a reconfigurable TXR suitable for TDD-LTE (even FDD-LTE, by duplicating the TXR as separated TX and RX modes). To build this concept, an SC gain loop is presented in Fig. 1(a). When a gain stage is rounded by an SC network that consists of a capacitor C_F and two switches, the primary functions of TX and RX are created. Empirically, "upmix + gain" is recognized as a TX function, as shown in Fig. 1(b), in which the BB signal is injected between the left-hand switch and C_F, while the RF signal is extracted from the gain stage's output. Based on the Miller effect, the extra downmix path helps reusing the gain stage to boost the effective C_F, and reduce the effective ON-resistance of the two switches. Besides, with the right-hand switch, a large RF impedance is seen at the gain stage's output, avoiding any unwanted gain drop. By transforming the SC network into an *N-path* SC network (see Section III), the gain-boosted N-path technique [10] can be embedded into such a gain loop, unifying the key TX functions in a closed-loop style: 1) signal amplification; 2) high-Q bandpass filtering; and 3) I/Q modulation.

The SC gain loop is reconfigurable as an RX by using the "gain + downmix" function, as shown in Fig. 1(c). Specifically, when the RF signal is injected at the gain stage's input, the BB signal can be extracted around C_F. Similar to the TX mode, the extra upmix path allows it to be compatible with the gain-boosted N-path technique. The resultant RX essentially offers the key functions: 1) signal amplification; 2) high-Q bandpass filtering; 3) I/Q demodulation; and 4) input-impedance matching. The details of RX mode will be given in Section IV.

III. N-Path SC Gain Loop as a TX

A. TX-Mode Architecture

As shown in Fig. 2, with $N = 4$, the N-path SC gain loop becomes a practical TX by adding four passive-*RC* filters $R_{BT}C_{BT}$ to receive the general four-phase BB signals $V_{BB,TX1-4}$ (i.e., differential and I/Q). Switches SW_L and SW_R perform the upmix and downmix functions, respectively, around the gain stage (G_{mRF}). G_{mRF} is an inverting amplifier that ensures the gain loop is under negative feedback. Outside

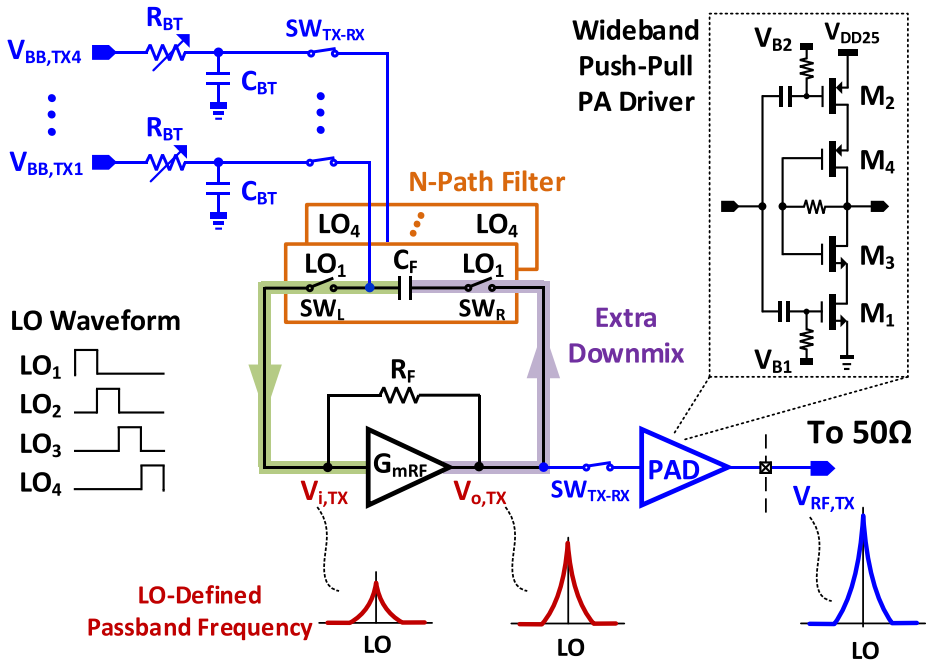

Fig. 2. Four-Path SC gain Loop as a TX. The four-phase BB ($V_{\mathrm{BB,TX1-4}}$) is injected via R_{BT}. The PAD extracts $V_{o,\mathrm{TX}}$ and drives the 50 Ω. Gain boosting the N-path filter by G_{mRF} realize high-Q bandpass responses at $V_{i,\mathrm{TX}}$ and $V_{o,\mathrm{TX}}$.

the gain loop, a wideband PAD is employed to boost the gain, provide isolation and drive the off-chip 50-Ω load.

When SW_L and SW_R are activated periodically by a four-phase non-overlap LO, the capacitor C_F is charged with an in-phase BB voltage at one side, while an amplified out-phased BB voltage is charged on the other side. As such, the effective capacitance of C_F at the input is boosted by the loop gain due to the Miller effect. This mechanism not only reduces the chip area for C_F, but also its parasitic effects, allowing the TX mode to operate at a higher RF. Another key aspect is that high-Q bandpass filtering is embedded at both $V_{i,\mathrm{TX}}$ and $V_{o,\mathrm{TX}}$ sharing one N-path SC network. Further, the IB RF voltage is summed in-phase over a switching period, while the OB RF voltage is canceled out at both $V_{i,\mathrm{TX}}$ and $V_{o,\mathrm{TX}}$. Unlike the typical passive N-path filter where the OB rejection is limited by the ON-resistance of the switches, here the loop gain offered by G_{mRF} alleviates such a limit due to the ON-resistance division by the open-loop gain (i.e., high OB rejection without consuming large LO power).

B. Functional View of the TX Mode

For intuitive understanding, a functional view of the TX mode is presented in Fig. 3(a). Note that it is *not* an equivalent circuit, since the "I/Q modulation" and "high-Q bandpass filtering" are unmerged as two cascaded functions to illustratively compare with [7]. The I/Q modulation is alike a typical TX, synthesizing an RF signal at $V_{i,\mathrm{TX}}$ from a four-phase BB signal at $V_{\mathrm{BB,TX1-4}}$. $V_{i,\mathrm{TX}}$ is virtually passed to a high-Q bandpass filter that can reject the OB noise first at $V_{i,\mathrm{TX}}$, and second at $V_{o,\mathrm{TX}}$. The N-path SC network can be modeled as a linear-time-invariant (LTI) *RLC* resonator around the passband [2], where the tunable inductor represents a tunable center frequency. Interestingly, when the extra downmix path in Fig. 2 is omitted, our closed-loop TX returns to an open-loop style similar to [7] that aims at low OB noise emission by direct-quadrature voltage modulation, as shown in Fig. 3(b). The narrowband PAD in [7] exploits a passive *LC* resonator for unwanted harmonics attenuation (<-40 dBc), and hence, the output response has a low Q and fixed center frequency. Unlike [7], here the gain created by G_{mRF} is reused to boost the Q of the bandpass responses at $V_{i,\mathrm{TX}}$ and $V_{o,\mathrm{TX}}$, resulting in much stronger OB noise suppression. To exemplify it, the simulated gain responses at $V_{i,\mathrm{TX}}$ and $V_{o,\mathrm{TX}}$ at 2 GHz are plotted, as shown in Fig. 4. Without the extra downmix path, $V_{i,\mathrm{TX}}$ offers only 11-dB OB rejection and no further improvement is added at $V_{o,\mathrm{TX}}$. For the proposed TX, the rejection at $V_{i,\mathrm{TX}}$ is improved to 22.5 dB, and an extra rejection of 7.8 dB is added at $V_{o,\mathrm{TX}}$. There is a 1.6-dB gain drop at $V_{o,\mathrm{TX}}$ in the TX, due to the finite frequency-translated impedance of the extra downmix path. Also, the gain response in Fig. 4 refers the four-phase BB to the single-phase RF. If considering the single-phase BB to the single-phase RF, the gain value is 9 dB higher. This fact applies to all plotted gain responses of the TX mode to be presented later.

C. TX-Mode Open-Loop Equivalent Model

To simplify the quantitative study, an *open-loop* equivalent model of the TX mode is developed, as shown in Fig. 5. Inspired by the principle of Miller decomposition, the N-path SC network can be subdivided into two parts referring to the gain stage's output and input. The former is alike a typical passive N-path filter [10] hanged on $V_{o,\mathrm{TX}}$, while the latter becomes four separated SC networks (i.e., single path, single phase) placed between the BB passive filter $R_{\mathrm{BT}}C_{\mathrm{BT}}$ and voltage mixer SW_L. The input-referred ON-resistance of

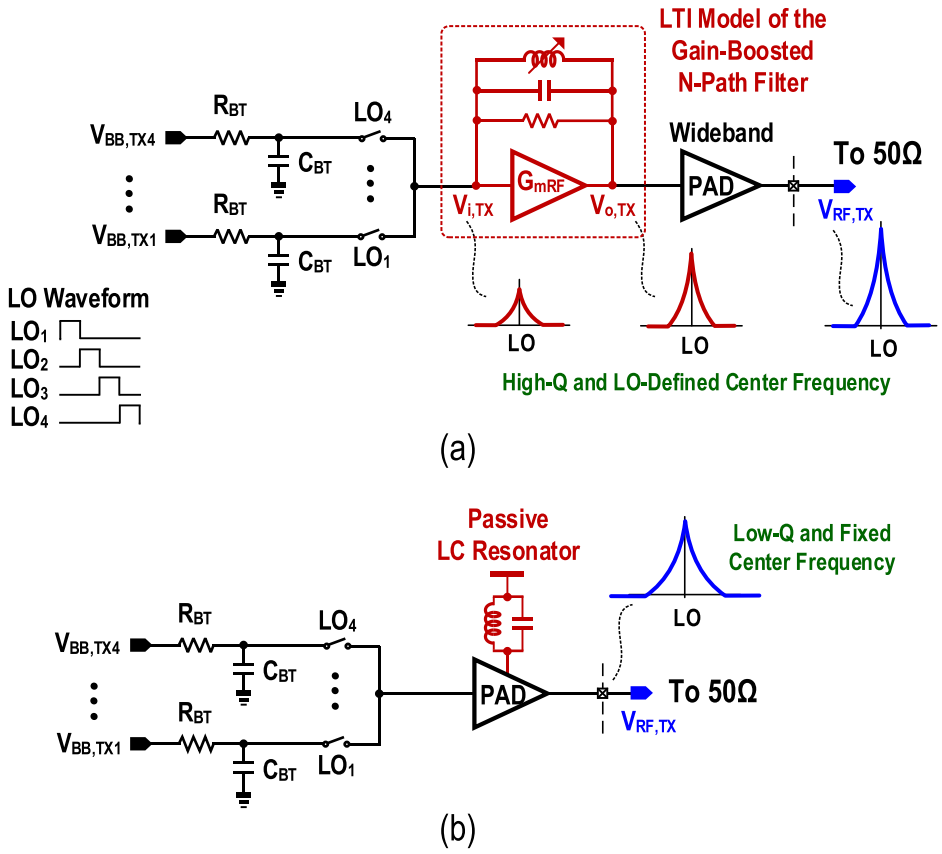

Fig. 3. (a) Functional view of the TX. It can be compared with [7] (b) that uses a passive *LC* resonator for its narrowband PAD. This work features a gain-boosted N-path filter and a wideband PAD to allow high-Q filtering and LO-defined center frequency, being more flexible for multiband operation.

SW_R ($R_{\mathrm{SWR},i}$) and the input-referred Miller capacitance of C_F ($C_{F,i}$) at BB are modeled

$$\begin{cases} R_{\mathrm{SWR},i} = \dfrac{R_{\mathrm{SWR}}//R_F + R_L}{1 + G_{\mathrm{mRF}} R_L} \\ R_{\mathrm{SWR},o} = \dfrac{R_{\mathrm{SWR}}//R_F + R_{\mathrm{SWR}}}{1 + G_{\mathrm{mRF}} R_{\mathrm{SWR}}} \\ C_{F,i} = \left| C_F \cdot \dfrac{(1 - G_{\mathrm{mRF}} R_F) R_L}{R_F + R_L} \right| \\ C_{F,o} = C_F \end{cases} \tag{1}$$

where $R_{\mathrm{SWR},o}$ is the output-referred switch's ON-resistance, $C_{F,o}$ is the Miller capacitance at $V_{o,\mathrm{TX}}$, and R_L is the load impedance of G_{mRF}. The modeled $C_{F,i}$ in (1) is equal C_F to multiplied by the open-loop gain of G_{mRF}. The enlarged $C_{F,i}$ implies less physical capacitors to realize a specific BW. For instance, with $G_{\mathrm{mRF}} = 130$ mS, $R_F = 9.3$ kΩ, $R_L = 38.4$ Ω, and $C_F = 8$ pF, the computed $C_{F,i}$ is 39.7 pF which is ∼5× more area efficient than the general passive N-path filter [2]. Also, the effective resistance $R_{\mathrm{SWR},i}$ (10 Ω) and $R_{\mathrm{SWR},o}$ (11.3 Ω) are both suppressed by G_{mRF}, improving the OB rejection.

To verify the accuracy of the model, the gain responses at $V_{i,\mathrm{TX}}$ are simulated at $R_{\mathrm{BT}} = 500$ Ω, as shown in Fig. 6(a), where the modeled open-loop response fits well with the closed loop, except that there is a 1.2-dB gain drop due to the input parasitic capacitance of G_{mRF}. The modeled gain response of the open-loop $V_{o,\mathrm{TX}}$ is accurate, as shown in Fig. 6(b), which has a better OB rejection (∼2 dB) as the far-out blockers see a smaller impedance at the open-loop $V_{o,\mathrm{TX}}$.

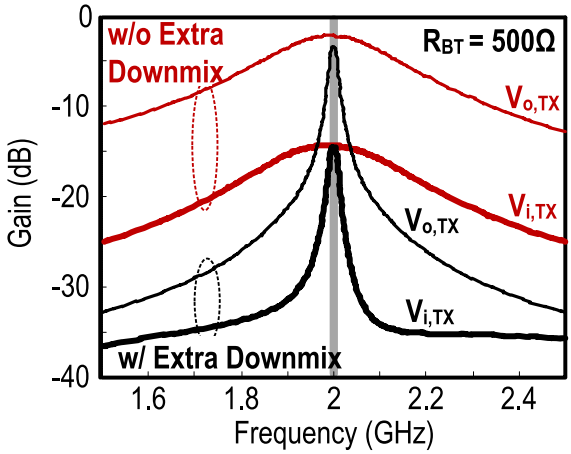

Fig. 4. Simulated TX-mode gain responses at $V_{i,\mathrm{TX}}$ and $V_{o,\mathrm{TX}}$ with and without the extra downmix path at 2 GHz.

D. Gain Response

Based on the open-loop equivalent model above, the gain response from BB to $V_{\mathrm{RF,TX}}$ can be studied in two steps. Recalling Fig. 5, the gain stage G_{mRF} essentially isolates its preceding and following stages, allowing the transfer function from BB to $V_{i,\mathrm{TX}}$ to be computed first, followed by that from $V_{i,\mathrm{TX}}$ to $V_{\mathrm{RF,TX}}$. For the former, a simplified equivalent circuit

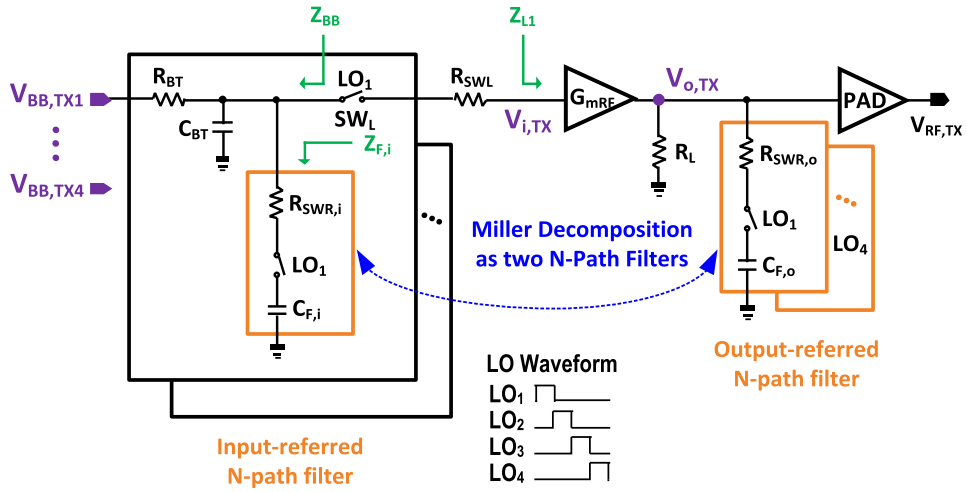

Fig. 5. Proposed open-loop TX model. The gain-boosted N-path filter is decomposed into two N-path filters using the principle of Miller decomposition [10]. R_F (9.3 kΩ) is large enough and can be omitted.

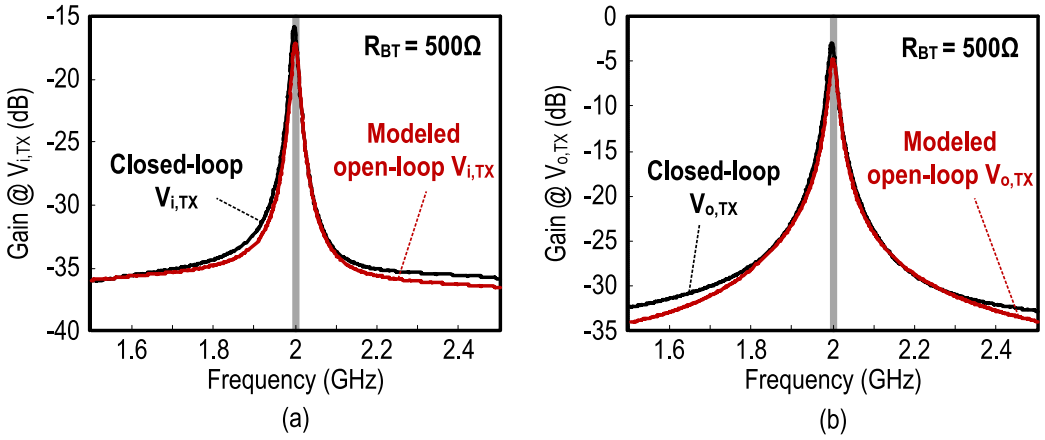

Fig. 6. Comparison of modeled and simulated gain responses. (a) Open-loop $V_{i,\mathrm{TX}}$ in Fig. 5 versus the closed-loop $V_{i,\mathrm{TX}}$ in Fig. 2. (b) Open-loop $V_{o,\mathrm{TX}}$ in Fig. 5 versus the closed-loop $V_{o,\mathrm{TX}}$ in Fig. 2.

is employed [Fig. 7(a)]. Since the input impedance seen from G_{mRF} is mainly capacitive (C_1), the load impedance is denoted by $Z_{L1}(\omega) = 1/jC_1$. Here, the angular frequency ω ω_{LO} is around. In view of the BB, the input voltage $V_{\mathrm{BB,TX1-4}}$ is in series with the BB impedance which is expressed as

$$Z_{\mathrm{BB}}(\omega-\omega_{\mathrm{LO}}) = R_{\mathrm{BT}} // \frac{1}{j(\omega-\omega_{\mathrm{LO}})C_{\mathrm{BT}}} // Z_{F,i}(\omega-\omega_{\mathrm{LO}}) \quad (2)$$

where $Z_{F,i}(\omega-\omega_{\mathrm{LO}})$ (Fig. 5) is the impedance of a single path decomposed from the extra downmix path. Since the SC circuit operates as a BB-to-BB gain response, the high-order frequency components can be ignored and $Z_{F,i}(\omega-\omega_{\mathrm{LO}})$ represented as

$$Z_{F,i} \approx 4R_{\mathrm{SWR},i} + \frac{1}{j(\omega-\omega_{\mathrm{LO}})C_{F,i}} \quad (3)$$

which enhances the BB rejection due to the boosted capacitance of $C_{F,i}$. Putting (3) into (2), $Z_{\mathrm{BB}}(\omega-\omega_{\mathrm{LO}})$ is expanded to

$$Z_{\mathrm{BB}}(\omega-\omega_{\mathrm{LO}}) = \frac{1}{1/R_{\mathrm{BT}} + j(\omega-\omega_{\mathrm{LO}})C_{\mathrm{BT}} + \frac{j(\omega-\omega_{\mathrm{LO}})C_{F,i}}{1+4R_{\mathrm{SWR},i}\cdot j(\omega-\omega_{\mathrm{LO}})C_{F,i}}}. \quad (4)$$

At center frequency with $\omega = \omega_{\mathrm{LO}}$, the impedance is R_{BT} in (4), and when ω moves away from ω_{LO} the impedance starts to roll-off. The −3 dB BW approaches $1/R_{\mathrm{BT}}(C_{\mathrm{BT}}+C_{F,i})$ if $R_{\mathrm{SWR},i}$ is nearly zero. In this case, the BB BW is dominated by $C_{F,i}$ and the ultimate rejection is infinite. If enlarging $R_{\mathrm{SWR},i}$, the −3 dB BW will be widened and finally converged to $1/R_{\mathrm{BT}}C_{\mathrm{BT}}$.

According to the LTI expression of the upconverted RF voltage in [12], the RF voltage $V_{i,\mathrm{TX}}$ transferred from $V_{\mathrm{BB,TX1-4}}$ in Fig. 7(a) can be obtained as

$$V_{i,\mathrm{TX}}(\omega) = \frac{\sqrt{2}}{\pi}\frac{Z_{L1}(\omega)\cdot Z_{\mathrm{BB}}(\omega-\omega_{\mathrm{LO}})/R_{\mathrm{BT}}}{Z_{L1}(\omega)+R_{\mathrm{SWL}}} \times \frac{e^{j\pi/4}\cdot V_{\mathrm{BB,TX1}}(\omega-\omega_{\mathrm{LO}}) + e^{-j\pi/4}\cdot V_{\mathrm{BB,TX2}}(\omega-\omega_{\mathrm{LO}})}{1+\frac{2}{\pi^2}Z_{\mathrm{BB}}(\omega-\omega_{\mathrm{LO}})\sum_{m=-\infty}^{+\infty}\frac{1}{(4m+1)^2(Z_{L1}(4m\omega_{\mathrm{LO}}+\omega)+R_{\mathrm{SWL}}}} \quad (5)$$

where m is an integer. In Fig. 8(a), (5) is plotted for 2 GHz which matches well with the simulated curve spanning from 1.5 to 2.5 GHz. The term of infinite summation in (5) is com-

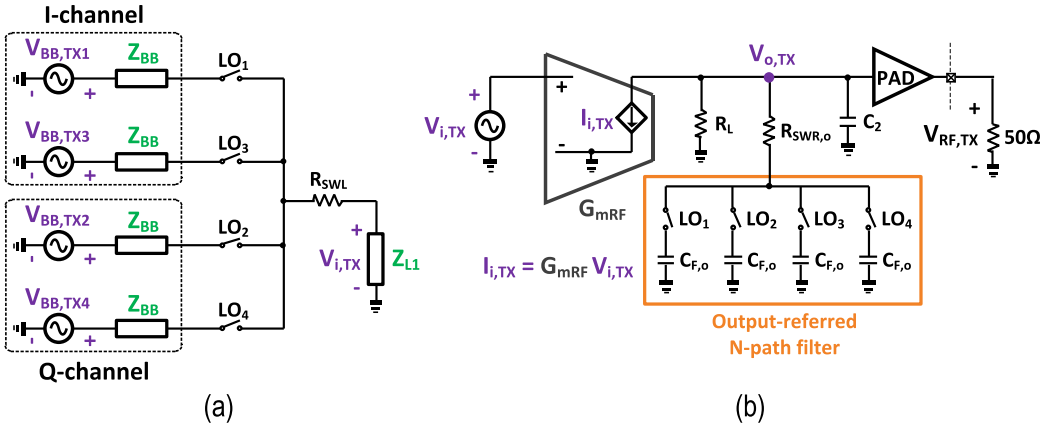

Fig. 7. Simplified circuit for calculating the responses. (a) From BB to $V_{i,\mathrm{TX}}$ of the open-loop TX. (b) From current source $I_{i,\mathrm{TX}}$ to $V_{\mathrm{RF,TX}}$. $I_{i,\mathrm{TX}}$ equals to the transconductance G_{mRF} multiplied by $V_{i,\mathrm{TX}}$.

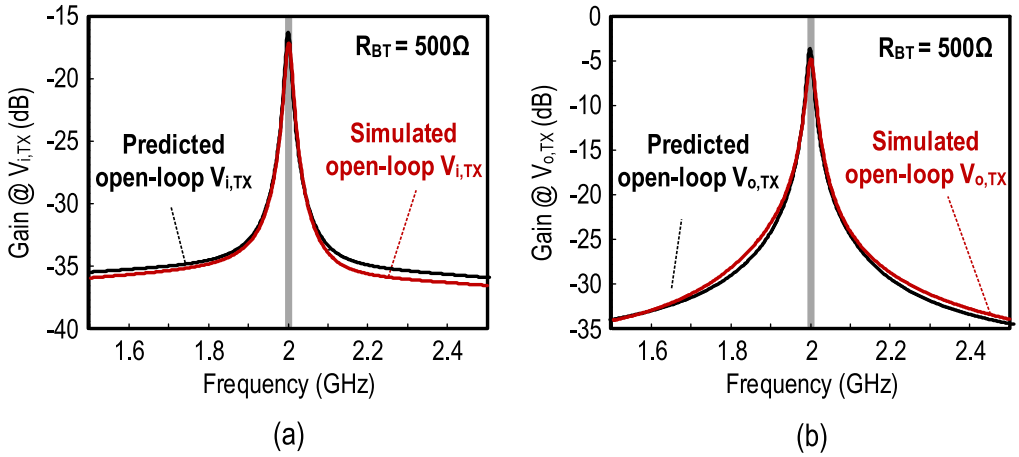

Fig. 8. Comparison of gain responses. (a) Simulated open-loop $V_{i,\mathrm{TX}}$ versus the approximation of (5). (b) Simulated open-loop $V_{o,\mathrm{TX}}$ versus the approximation of (8).

posed by the fundamental and higher odd-order harmonics. Since the fundamental term is dominant, (5) can be simplified as

$$V_{i,\mathrm{TX}}(\omega) \approx \frac{\sqrt{2}}{\pi}\frac{Z_{L1}(\omega)\cdot Z_{\mathrm{BB}}(\omega-\omega_{\mathrm{LO}})/R_{\mathrm{BT}}}{Z_{L1}(\omega)+R_{\mathrm{SWL}}+\frac{2}{\pi^2}Z_{\mathrm{BB}}(\omega-\omega_{\mathrm{LO}})} \times (e^{j\pi/4}\cdot V_{\mathrm{BB,TX1}}(\omega-\omega_{\mathrm{LO}}) + e^{-j\pi/4}\cdot V_{\mathrm{BB,TX2}}(\omega-\omega_{\mathrm{LO}})) \quad (6)$$

where $V_{i,\mathrm{TX}}(\omega)$ provides an intuitive view of the lowpass response of $Z_{\mathrm{BB}}(\omega-\omega_{\mathrm{LO}})$ upconverted to $V_{i,\mathrm{TX}}$ as a high-Q bandpass response, with a -3 dB BW around twice of that from (4).

Similarly, to analyze the response from $V_{i,\mathrm{TX}}$ to $V_{\mathrm{RF,TX}}$ of the open-loop TX model a simplified circuit is developed, as shown in Fig. 7(b), where G_{mRF} is modeled as a transconductor converting the input $V_{i,\mathrm{TX}}$ to output current $I_{i,\mathrm{TX}}$ and is expressed as $I_{i,\mathrm{TX}} = G_{\mathrm{mRF}}V_{i,\mathrm{TX}}$. C_2 is the input parasitic capacitance of PAD. $I_{i,\mathrm{TX}}$ draws current from R_L, C_2 and the output-referred N-path filter to create the RF voltage $V_{o,\mathrm{TX}}$. As the PAD involves no frequency translation and its passband gain should be flat, our focus is on the response from $V_{i,\mathrm{TX}}$ to $V_{o,\mathrm{TX}}$. Referring to [13], the impedance $Z_{o,\mathrm{TX}}(\omega)$ seen by $V_{o,\mathrm{TX}}$ is

$$Z_{o,\mathrm{TX}}(\omega) = \frac{R_{\mathrm{SWR},o}\cdot Z_{L2}(\omega)}{R_{\mathrm{SWR},o}+Z_{L2}(\omega)} + \frac{\left(\frac{Z_{L2}(\omega)}{R_{\mathrm{SWR},o}+Z_{L2}(\omega)}\right)^2\cdot\frac{2}{\pi^2}Z_{F,o}(\omega-\omega_{\mathrm{LO}})}{1+\frac{2}{\pi^2}Z_{F,o}(\omega-\omega_{\mathrm{LO}})\sum_{m=-\infty}^{+\infty}\frac{1}{(4m+1)^2(Z_{L2}(4m\omega_{\mathrm{LO}}+\omega)+R_{\mathrm{SWR},o})}} \quad (7)$$

where $Z_{L2}(\omega) = R_L//(1/(j\omega C_2))$ and $Z_{F,o}(\omega-\omega_{\mathrm{LO}}) = (1/(j(\omega-\omega_{\mathrm{LO}})C_{F,o}))$. Thus, $V_{o,\mathrm{TX}}$ is deduced as

$$V_{o,\mathrm{TX}}(\omega) = G_{\mathrm{mRF}}Z_{o,\mathrm{TX}}(\omega)\cdot V_{i,\mathrm{TX}}(\omega). \quad (8)$$

As shown in Fig. 8(b), the prediction from (8) fits well with the simulations covering a 1-GHz span at LO = 2 GHz. If the higher harmonics are ignored, (7) is simplified to a high-Q bandpass impedance as in the following equation:

$$Z_{o,\mathrm{TX}}(\omega) = \frac{Z_{L2}(\omega)}{Z_{L2}(\omega)+R_{\mathrm{SWR},o}}\cdot\left(R_{\mathrm{SWR},o}+\frac{Z_{L2}(\omega)}{1+j\frac{\pi^2}{2}C_{F,o}(R_L+R_{\mathrm{SWR},o})(\omega-\omega_{\mathrm{LO}})}\right). \quad (9)$$

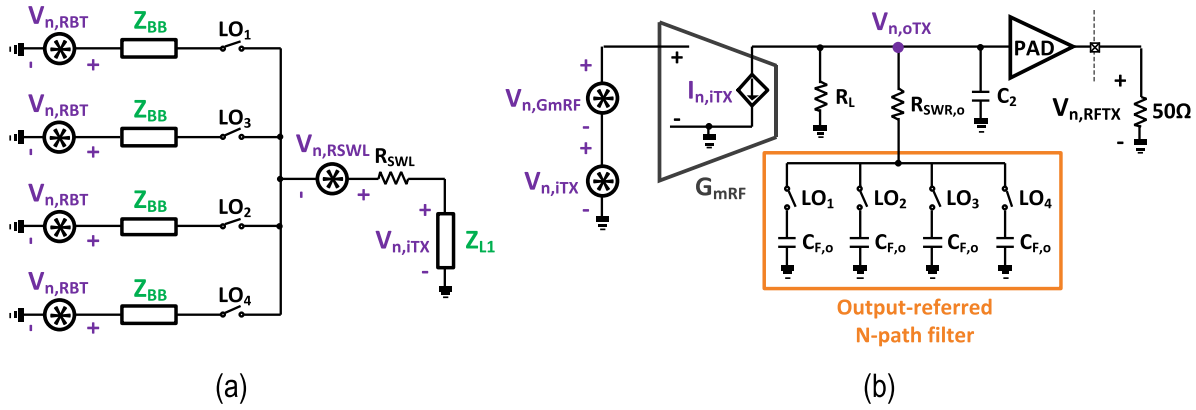

Fig. 9. Simplified equivalent circuit for noise analysis of (a) $R_{\rm BT}$ and $\rm SW_L$ and (b) $G_{\rm mRF}$.

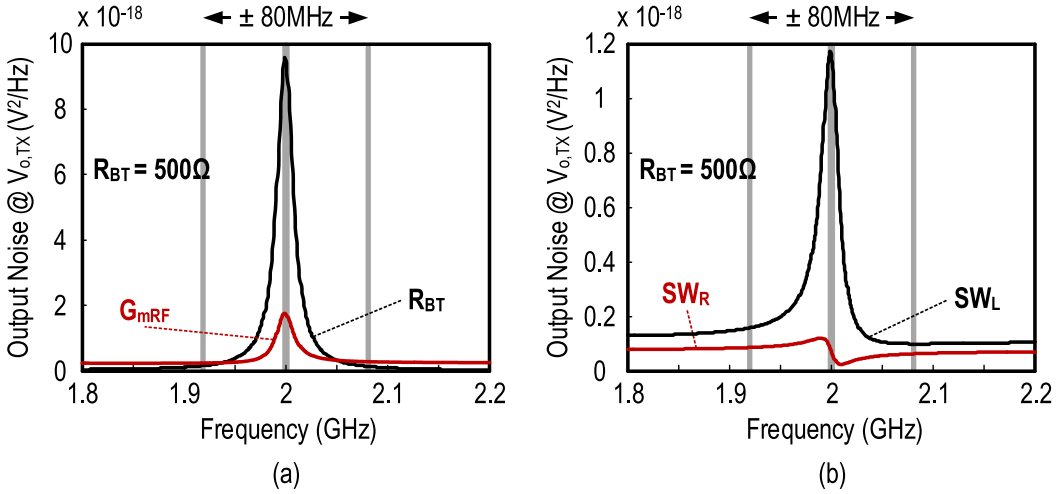

Fig. 10. Simulated output noise power at $V_{o,\rm TX}$ with contribution from (a) $R_{\rm BT}$ and $G_{\rm mRF}$ and (b) $\rm SW_L$ and $\rm SW_R$.

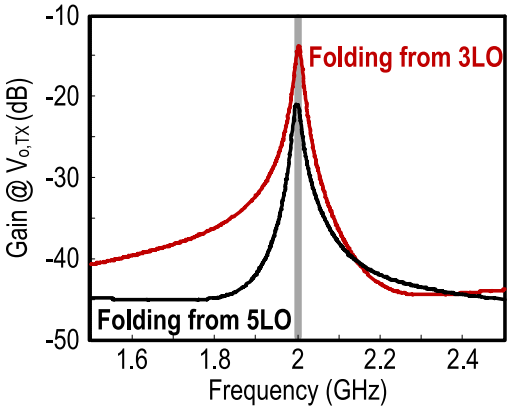

Fig. 11. Simulated unwanted folding terms from 3 LO and 5 LO at $V_{o,\rm TX}$.

At the center frequency, (9) equals to $Z_{L2}(\omega)$, and it is interesting that the output-referred N-path load does not bring any gain drop if the harmonics are out of concern [13]. However, the parasitic capacitance C_2 induces a $1/(1+j\omega R_L C_2)$ gain drop (e.g., -0.6 dB at 2 GHz). Also, the -3 dB BW of the high-Q bandpass filtering equals to $4/\pi^2 C_{F,o}(R_L + R_{\rm SWR,o})$ when $Z_{L2}(\omega)$ is resistive.

E. Noise Analysis

Most OB noise of the TX mode is due to the thermal noise of $R_{\rm BT}$, gain stage $G_{\rm mRF}$, and ON-resistance $R_{\rm SWL}$. As modeled in Fig. 9(a), the thermal noise voltage $V_{n,\rm RBT}$ is in series with the BB impedance and experiences the same transfer function of the BB signals. As such, the power spectral density (PSD) at $V_{n,o\rm TX}$ due to $R_{\rm BT}$ is

$$\overline{V^2_{n,R_{\rm BT},o\rm TX}} = |H_{i,\rm TX}|^2 \cdot |H_{o,\rm TX}(\omega)|^2 \cdot \overline{V^2_{n,R_{\rm BT}}} \tag{10}$$

where $|H_{i,\rm TX}(\omega)|$ and $|H_{o,\rm TX}(\omega)|$ are introduced as the transfer functions from BB to $V_{i,\rm TX}$ and $V_{i,\rm TX}$ to $V_{o,\rm TX}$, respectively, to represent (5) and (8). The thermal noise power of $R_{\rm BT}$ is $\overline{V^2_{n,R_{\rm BT}}} = 4kTR_{\rm BT}$. The OB noise contribution from $R_{\rm BT}$ is greatly suppressed because of the high-Q bandpass filtering in the N-path SC gain loop. Similarly, the output noise PSD due to $R_{\rm SWL}$ is

$$\overline{V^2_{n,R_{\rm SWL},o\rm TX}} = \left(\frac{R_{\rm BT}}{Z_{\rm BB}(\omega-\omega_{\rm LO})}\right)^2 \cdot |H_{i,\rm TX}(\omega)|^2 \cdot |H_{o,\rm TX}(\omega)|^2 \cdot \overline{V^2_{n,R_{\rm SWL}}} \tag{11}$$

where $\overline{V^2_{n,R_{\rm SWL}}} = 4kTR_{\rm SWL}$. As shown in Fig. 9(b), the thermal voltage source of the $G_{\rm mRF}$ stage is modeled as an

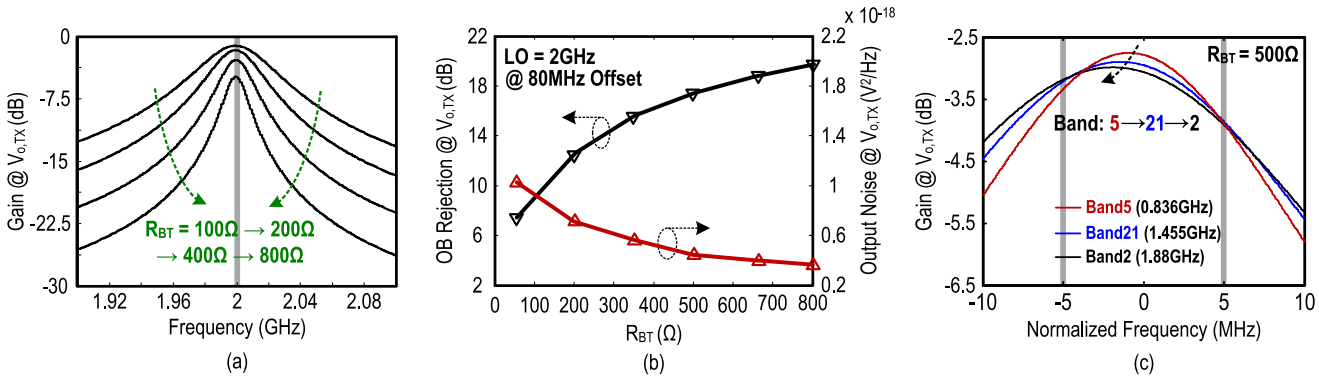

Fig. 12. (a) R_{BT} should balance the signal BW, OB rejection, and noise. (b) Output OB noise reduces with increased OB rejection, but it will saturate as a large R_{BT} induces noise itself. (c) When RF frequency increases from 0.836 to 1.88 GHz, passband frequency shifting increases from 0.9 to 1.9 MHz while the gain droop decreases from 1.1 to 0.8 dB.

input-referred $V_{n,G\mathrm{mRF}}$, and the corresponding noise power is $\overline{V^2_{n,G\mathrm{mRF}}} = 4kT/G_{\mathrm{mRF}}$. $V_{n,G\mathrm{mRF}}$ experiences the same transfer function as $V_{n,i\mathrm{TX}}$, and thus, the output noise PSD due to G_{mRF} is

$$\overline{V^2_{n,G\mathrm{mRF},o\mathrm{TX}}} = |H_{o,\mathrm{TX}}(\omega)|^2 \cdot \overline{V^2_{n,G\mathrm{mRF}}}. \tag{12}$$

The simulated output noises at $V_{o,\mathrm{TX}}$ due to R_{BT} and G_{mRF} are shown in Fig. 10(a), and due to SW_L and SW_R are shown in Fig. 10(b). When the offset frequency is beyond 70 MHz, G_{mRF} generates more noise than that of R_{BT} as it experiences less OB rejection within the N-path SC gain loop. When comparing it with SW_L, SW_R contributes with a less noise due to the lack of amplification in the extra downmix path (Fig. 2). Furthermore, the output noises shown in Fig. 10 are almost flat when the offset frequency is referred to over 80 MHz. Upsizing the switches $\mathrm{SW}_{L,R}$ can achieve a lower output noise floor, at the expense of more LO power.

The simulated harmonic-folding effect at $V_{o,\mathrm{TX}}$ is shown in Fig. 11. For $N = 4$, the nearest and strongest component that folds back to the desired band (around LO) is 3xLO, and after is 5xLO [12]. Even though the TX is single-ended, the even harmonic folding is insignificant (simulated <-70 dB). Due to the high-Q bandpass filtering of the gain-boosted N-path technique around 3xLO and 5xLO, the far-out noise induced by the folding terms is much smaller than the IB that experiences no frequency translation. Thus, the harmonic-folding effect is generally less important in the TX design.

F. OB Noise, Passband Roll-Off, and Harmonic Emission

The BB resistor plays a key role in balancing the performances in terms of signal BW, voltage gain, OB linearity, and OB noise. Intuitively, any resistors coupled to the N-path SC gain loop will degrade the Q of the passband responses at $V_{i,\mathrm{TX}}$ and $V_{o,\mathrm{TX}}$. A large R_{BT} improves the OB rejection, but at the expense of a gain drop in the passband due to the finite input impedance at $V_{i,\mathrm{TX}}$, as shown in Fig. 12(a). Simulated at 2 GHz, with R_{BT} ranging from 100 to 800 Ω, the OB rejection increases but induces a 4-dB gain drop, whereas the -1 dB BW decreases from 24 to 8 MHz. The output noise at $V_{o,\mathrm{TX}}$ drops from 1.04 to 0.33 aV^2/Hz at 80-MHz offset owing to the increased rejection from 7.3 to 19.3 dB, as shown in Fig. 12(b). In fact, as R_{BT} generates noise itself, the rejection of OB noise will be saturated eventually if raising only R_{BT}. Here, our TX mode chooses a 500-Ω R_{BT} to achieve 17.1-dB OB rejection and 0.42-aV^2/Hz output noise at $V_{o,\mathrm{TX}}$. From SpectreRF simulations (pss + pnoise), the OB noise at $V_{\mathrm{RF,TX}}$ is -157.7 dBm/Hz at 80-MHz offset, whose main contributors are R_{BT} (24%), G_{mRF} (20%), $\mathrm{SW}_{L,R}$ + LO divide-by-4 circuitry (20%) and PAD (10%). The rest arising from the off-chip 50-Ω load and switches $\mathrm{SW}_{\mathrm{TX-RX}}$ for the TX–RX mode control.

Mainly due to the input capacitor of G_{mRF}, the simulated passband frequency shifting is within 0.9 to 1.9 MHz when the RF frequency covers between 0.836 (Band5) to 1.88 GHz (Band2), as shown in Fig. 12(c), with 1.1-dB passband roll-off at Band5, and 0.8 dB at Band2 for LTE10. The impact of such roll-off characteristics on the EVM performance should be insignificant, since the EVM of an LTE signal is the RMS value of each Resource Block (RB)'s EVM and the BW (180 kHz) of each RB is much smaller than the signal BW (9 MHz for LTE10) [14]. If addressing this roll-off issue, a pre-emphasis digital equalizer can be applied to compensate the passband roll-off for the TX mode, similar to the post-emphasis equalizer used in the RX path [15]. In the digital baseband, the compensation of different passband roll-offs (0.3-dB range) according to the RF frequency is feasible at the cost of small area and power. In addition, the pre-emphasis digital equalizer can be an option to compensate the sharp roll-off region of analog filter for [8], although without passband frequency shifting.

For the spectral purity, $V_{o,\mathrm{TX}}$ contains typical LO harmonic emission with a third-order harmonic-rejection ratio (HRR_3) of 9.5 dB for $N = 4$. Nevertheless, with the limited BW of the PAD and output bonding wire, the HRR_3 at the TX output $V_{\mathrm{RF,TX}}$ is improved, as shown in Fig. 13, and goes up with frequency (e.g., 23 dB at 2 GHz). In addition, the second-order harmonic distortion (HD_2) at $V_{\mathrm{RF,TX}}$ is dominated by the single-ended PAD operating in class-AB mode. In fact, by properly matching the PAD's push-pull transistors, HD_2 can be <-37 dBc at a 0-dBm P_{out} from simulations (Fig. 13). Harmonic-rejection N-path filtering [16] can be an option to further improve the harmonic emission. In practice, the output of PAD is loaded by an off-chip PA. For LTE applications, the

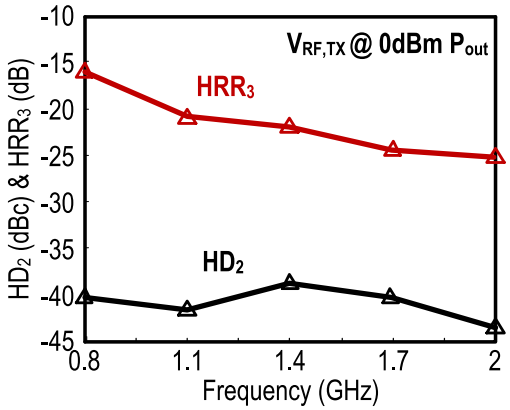

Fig. 13. Simulated OB harmonics (HD_2 and HRR_3) at $V_{RF,TX}$ versus operating frequency.

commercial high-power PA (see [17]) is narrowband and will suppress all OB harmonics from its TX. Thus, the spectrum clearance at the final output should still be dominated by the PA harmonic distortion. Finally, a single-pole multi-throw switch can be used for the multiband TX to interface with different PAs.

G. Other Implementation Details

To enhance the power efficiency and avoid any internal gain nodes, G_{mRF} was chosen as an inverter-based amplifier self-biased by a feedback resistor R_F. The non-overlap LO_1–LO_4 (25% duty cycle) prevents the I/Q crosstalk from degrading the linearity. The capacitor C_{BT} essentially operates as a charge buffer at the BB side to relieve the gain drop at the RF side, due to the input capacitance of G_{mRF}. By switching $SW_{L,R}$, the filtered BB voltages will be up-sampled to $V_{i,TX}$ in sequence, thus seeing a high-input impedance of G_{mRF} and allowing good linearity. In order to decouple the signal-handing ability of G_{mRF} to the overall TX output power, the RF signal at $V_{o,TX}$ is further amplified by the wideband single-ended PAD before outputting $V_{RF,TX}$. The PAD is based on a push-pull cascode structure (M_{1-2}) and with the cascode transistors (M_{3-4}) self-biased by a feedback resistor (Fig. 2). From simulations, the class-AB PAD achieves a -1 dB output BW of $\sim$2.1 GHz, which is adequate to cover $>$80% of the LTE-TDD/FDD bands from 0.7 to 2 GHz. As the PAD is single-ended, a 2.5-V supply allows better HD_3 (-43.4 dBc) and voltage gain (9.3 dB) while showing a 12.2% drain efficiency at a 0-dBm single-tone P_{out}. Both HD3 (-37 dBc) and voltage gain (5.7 dB) will be degraded if a 1.2-V supply is applied and the cascode transistors are removed.

As a reconfigurable TXR, the TX–RX mode switches (Fig. 2) are critical and should be carefully sized to minimize the parasitic effects, especially for the PAD that has an input capacitance of $\sim$500 fF. When the PAD is power down, $V_{B1} = \text{GND}$ and $V_{B2} = V_{DD25}$ (2.5 V) are set for M_1 and M_2, respectively, to share the voltage stress between M_{1-4} to ensure the device reliability [18].

Unlike the gain-boosted mixer-first RX in [6] that benefits from a large G_{mRF} (200 mS) to improve the NF and OB linearity, here G_{mRF} is downsized to 130 mS with the concerns of spectral regrowth and EVM in the TX mode. In addition, [6] employs a 0.7-V supply for power savings, but entailing large transistors to generate a 200-mS G_{mRF}, which strongly restricts the RF coverage due to large parasitic capacitance. Here, the parasitic capacitance is designed to be 2.2$\times$ smaller than [6]. The loop gain offered by G_{mRF} reduces the physical size of C_F to 8 pF for our targeted signal BW of $\sim$12 MHz. As the PAD isolates the N-path SC gain loop with the external parts (e.g., bondwire and pad), the center frequency of the passband is defined by the LO.

IV. N-Path SC Gain Loop as an RX

The four-path SC gain loop can be reconfigured as a multiband RX as depicted in Fig. 14(a), which is compatible with the TX mode without tuning of components. Since SW_L and C_F are already embedded in the downmix process, the original switch SW_R in the SC gain Loop (Fig. 2) can be disabled in the RX mode [6]. The RF signal $V_{RF,TX}$ at the source port is injected at the input of G_{mRF} ($V_{i,RX}$), and after amplification, the RF signal is down-converted as four-phase BB signals extracted by series switches SW_B that are driven by a set of out-phased LO. Finally, the four-path BB signals are amplified ($V_{BB,RX1-4}$) by an inverter-based transconductance amplifier (G_{mBB}), where the channel length of transistors is set at 0.18 μm to reduce the flicker noise. G_{mBB} is sized as 11 mS. The theory of the gain-boosted N-path RX is detailed in [10] and [11].

Due to the bidirectional transparency property of N-path passive mixers, the RX can achieve input matching over a wide range of RF without any off-chip matching components. As shown in Fig. 14(a), an LO-defined bandpass input impedance can be created at $V_{i,RX}$ by frequency-translating the BB lowpass response to RF as bandpass, via the passive mixer SW_L. Besides, the mixer SW_L, at the extra upmix path, also creates an N-path filter around G_{mRF} with the feedback capacitor C_F together, resulting in high-Q bandpass filtering at both $V_{i,RX}$ and $V_{o,RX}$, as shown in Fig. 14(b). Thanks to the loop gain created by G_{mRF}, the BB circuitry sees a higher impedance back to the source port [19], allowing the use of large R_{BR} (21 kΩ) and small C_{BR} (1 pF) to save the die area and improve the NF.

Thanks to G_{mRF} that offers phase inversion between its input and output, the frequency shifting of the S_{11}-BW from the LO due to the input capacitance (imaginary part) is alleviated to $<$1 MHz [6]. In contrast, the simulated frequency shifting raises to $\sim$5 MHz for the typical passive mixer-first RX [4]. The series inductance (bondwire) can be as large as 1.9 nH when targeting a $S_{11} < -10$ dB, which is within the practical range and can help to lower the NF by 0.4 dB in virtue of enhancing the passband gain, while suppressing harmonic-folding terms [20]. The simulated passband frequency shifting ranges from 0.3 to 0.8 MHz when the RF frequency covers from 0.836 (Band5) to 1.88 GHz (Band2), as shown in Fig. 14(c), and the passband roll-off ranges from 1.6 to 1.9 dB. Compared to the TX mode, here the passband ripple is $\sim$1 dB higher due to the impact of BB impedance, which can be addressed by the post-emphasis digital equalizer [15].

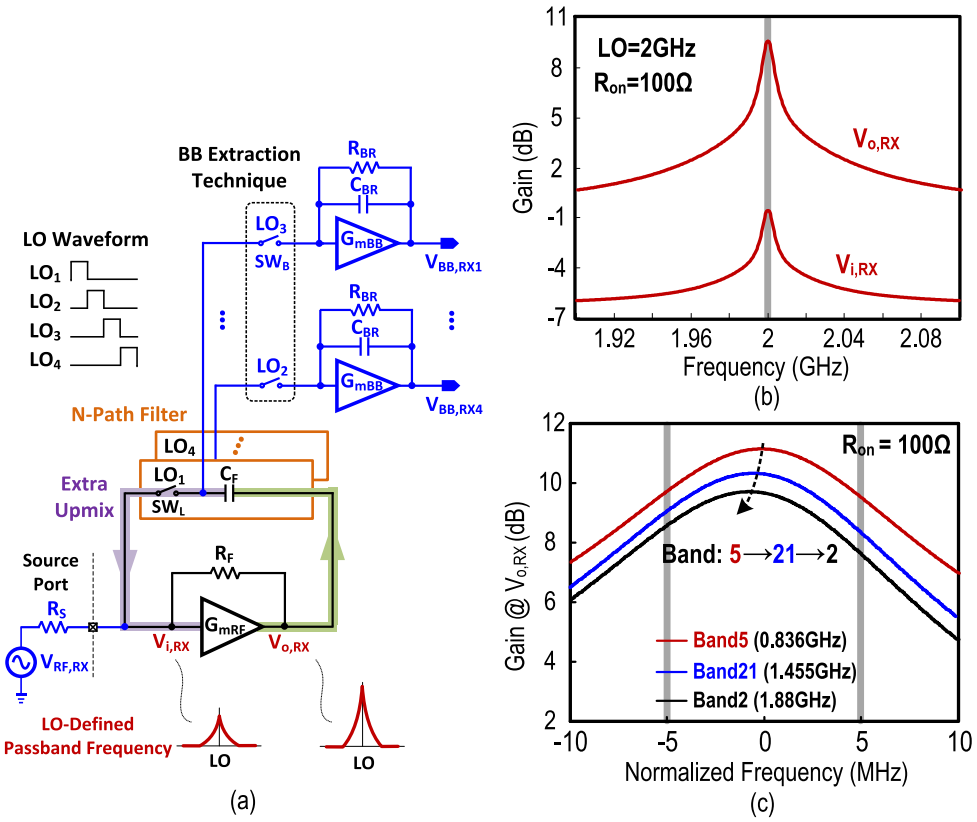

Fig. 14. (a) *Four-path SC gain Loop* as a RX. The four-phase BB is extracted via SW_B driven by a 25% LO out-phased with the N-path filter, avoiding the BB noise from leaking to the source port (i.e., better NF). $SW_L + C_F$ are already embedded in the downmix function [6]. (b) Simulated gain responses at $V_{i,RX}$ and $V_{o,RX}$. (c) Passband frequency shifting increases from 0.3 to 0.8 MHz when the RF band ranges from Band5 to Band2, and the passband gain droop increases from 1.6 to 1.9 dB.

As the input-impedance matching is provided by the BB impedance frequency-translated to the RF port [6], a large (9.3 kΩ) is allowed to concurrently improve the gain, NF, and OB rejection. The BW of the BB lowpass response is mainly defined by R_{BR} and C_{BR}.

For the BB extraction, unlike the RX in [6] that exploits series resistors R_1 (Fig. 2.4.2a), here switches SW_B in series with the BB amplifiers are employed [Fig. 14(a)]. SW_B are driven by the same 25%-duty-cycle LO, but are out-phased with those in the N-path filter, to prevent the BB noise from leaking directly to the antenna port (only leaking to the output of G_{mRF}), resulting in a better NF. As shown in Fig. 15, the simulated OB rejection and NF are plotted for two different BB-extraction techniques at 2 GHz. In Fig. 15(a), the NF is optimized to 3.12 dB when the BB series resistor R_1 is set at 100 Ω. Smaller R_1 will induce a higher gain drop, whereas a large R_1 will generate additional noise from itself. In this paper [Fig. 15(b)], the NF is improved to 1.84 dB when the ON-resistance R_{SWB} of the out-phased switch SW_B is sized at the same 100 Ω. Besides, both BB-extraction techniques provide similar OB rejection at both $V_{i,RX}$ and $V_{o,RX}$.

V. Four-Phase LO Generator and TX/RX-Mode Logics

A div-by-4 ring counter generates the four-phase LO, as shown in Fig. 16. To achieve high LO phase precision at low power, the dynamic D flip-flops are based on transmission gates, and a phase corrector is added after the first input buffer which receives the off-chip differential master clock ($4LO_P$ and $4LO_N$) running at 4× LO. Due to the reconfigurability of the TXR, a TX/RX-mode logic block is added to activate or disable the switches SW_L, SW_R, and SW_B. For the TX mode, $LO_{1-4,SWL}$ and $LO_{1-4,SWR}$ are driven by the four-phase LO, while switch SW_B is OFF. For the RX mode, switch is SW_R ON, while $LO_{1-4,SWL}$ and $LO_{1-4,SWB}$ share the same four-phase LO but are out-of-phase to each other. By properly sizing and determining the transistors' ratios in the output buffers and TX/RX-mode logic block, the non-overlap LO is robustly generated against PVT variations. The simulated LO phase noise at 2 GHz is −159.8 and −160.7 dBc/Hz at 80-MHz offset for TX and RX modes, respectively. The LO generator at 2 GHz draws 10.3 mA (7 mA) in the TX (RX) mode.

VI. Measurement Results

The TXR prototype was fabricated in 65-nm CMOS. Without inductors or baluns, the TXR occupies a very small die area (0.038 mm^2) which is dominated by the four-path feedback capacitors (32 pF) and PAD, as shown in Fig. 17. The TX and RX modes operate separately and are controlled by switches SW_{TX-RX}.

A. TX Mode

G_{mRF} and the LO generator are powered at 1.1 V, while the PAD is powered at 2.5 V. The measured output

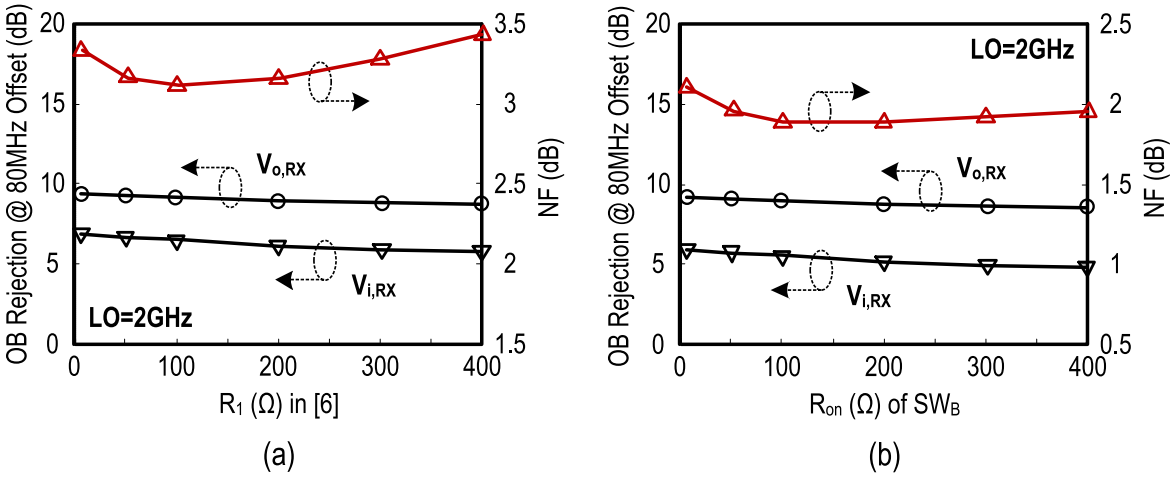

Fig. 15. Simulated OB rejection at $V_{i,\mathrm{RX}}$ and $V_{o,\mathrm{RX}}$ and NF versus (a) BB series resistors R_1 in [6], and (b) ON-resistance R_{SWB} of the out-phased switches SW_B at 2 GHz.

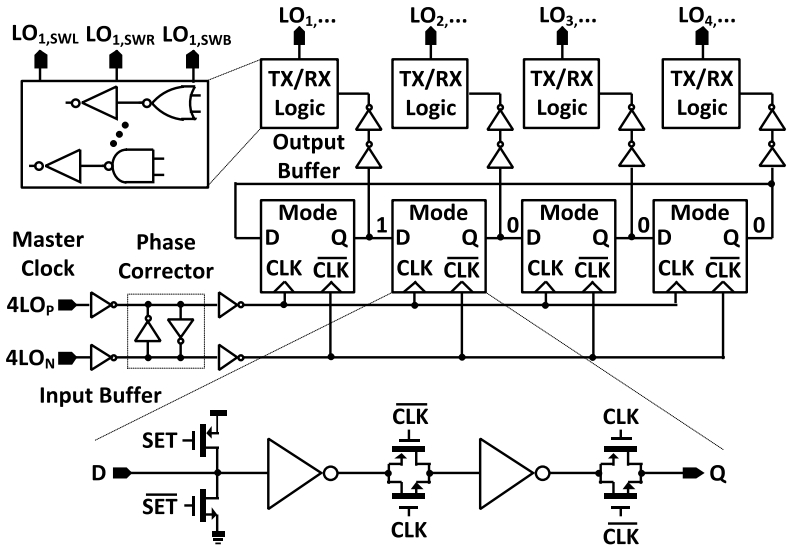

Fig. 16. 25%-duty-cycle four-phase LO generator with TX/RX-mode switch logics.

spectrum of a 10-MHz-BW 64-quadratic-amplitude modulation OFDM signal at the LTE Band2 (1.88 GHz) is depicted in Fig. 18. The $\mathrm{ACLR}_{\mathrm{EUTRA1}}$ and $\mathrm{ACLR}_{\mathrm{EUTRA2}}$ are -40 and -51.9 dBc, respectively, at a -1 dBm output power after de-embedding the loss of the cable and PCB. The EVM is 2%. By adjusting the gain-phase balancing of $V_{\mathrm{BB,TX1-4}}$, the spurs due to I/Q mismatch and LO feedthrough are suppressible to <-40 dBc. By simply sweeping the LO frequency, high-Q bandpass responses are consistently measured at different RF consistent with the simulations [Fig. 19(a)]. The noise floor is -154.5 dBc/Hz at 80-MHz offset for Band2 as shown in Fig. 19(b), which includes the thermal noise of the TX path, and phase noise of the LO generator. Similar results are measured at LTE Band5 (0.836 GHz at 45-MHz offset) and Band21 (1.455 GHz at 48-MHz offset). At a -1 dBm output power, CIM_3 and CIM_5 are <-49 and <-63 dBc, respectively, as shown in Fig. 19(a).

The power consumption is dominated by the PAD (16.3 mW), G_{mRF} (10.8 mW), and LO generator (11.3 mW) at the LTE Band2. As shown in Fig. 20(a), the power consumption rises from 31.3 (Band5) to 38.4 mW (Band2) due to the dynamic type of the LO generator that has an average power efficiency of ~6.6 mW/GHz. The TX-mode power consumption downscales accordingly when the output power is back off as shown in Fig. 20(b) for Band2 and Band5. For example, at a 3-dB power back off, the power consumption at Band2 (Band5) drops by 5.1 mW (4.8 mW) which is mainly associated with the PAD. The power saving is <15% as the 3-dB power back off is only based on the gate biases ($V_{B1,2}$) of the PAD. A more power-efficient variable-gain PAD should be explored as it can operate out of the N-path SC gain loop.

The performance summary is given in Table I and is benchmarked with the state-of-the-art current-/voltage-mode LTE TXs [8], [21]. Thanks to the effective gain-boosted

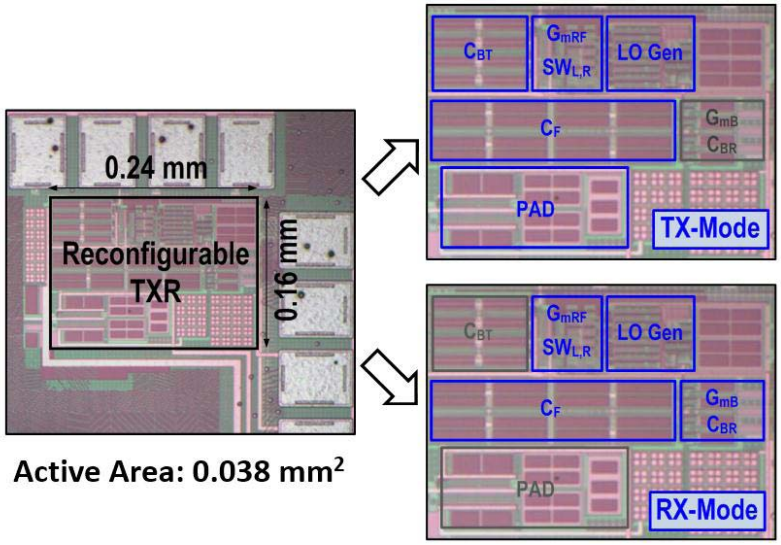

Fig. 17. Chip photograph of the TXR that can be reconfigured as a TX or RX by simple mode switching.

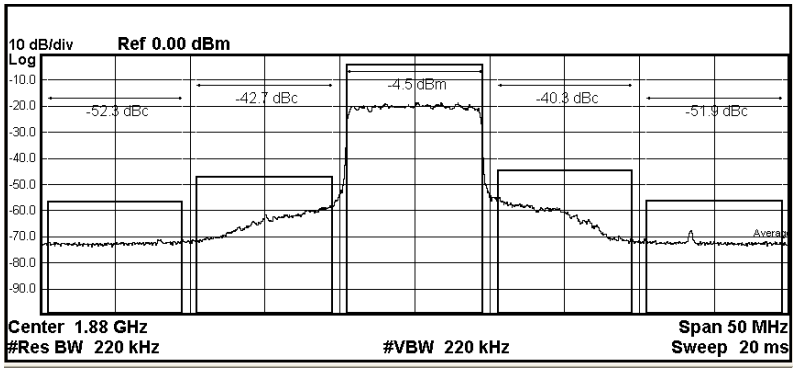

Fig. 18. TX-mode: Output spectrum of a 10-MHz BW 64-QAM OFDM signal at the LTE Band2.

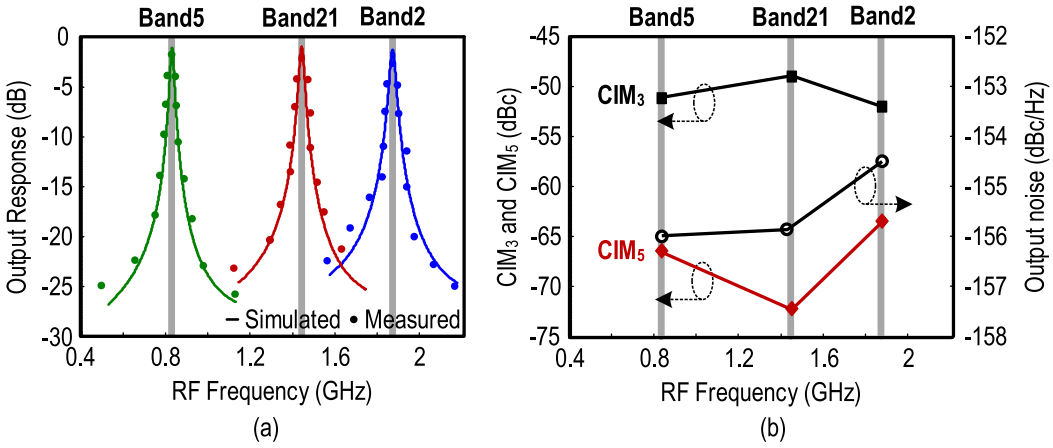

Fig. 19. TX mode. (a) LO-defined bandpass responses at different LTE bands (matched with simulations). The output response (0 dB) is referred to a 0-dBm P_{out}. (b) $CIM_{3,5}$ at 5-MHz BB frequency and OB noise.

N-path filtering, this work succeeds in improving the multi-band flexibility and area efficiency that is 24× better than the state-of-the-art, while preserving a comparable power efficiency (2.1% for Band2 and 2.4% for Band5). However, the output noise is inferior when compared with [8] that concentrates the power budget on the final power mixer stage and [21]. We also acknowledge that [8] and [21] have a higher output power and better spectral purity under a higher power budget.

B. RX Mode

A single 1-V supply is employed for the RX mode. In Fig. 21(a), narrowband input-impedance matching is

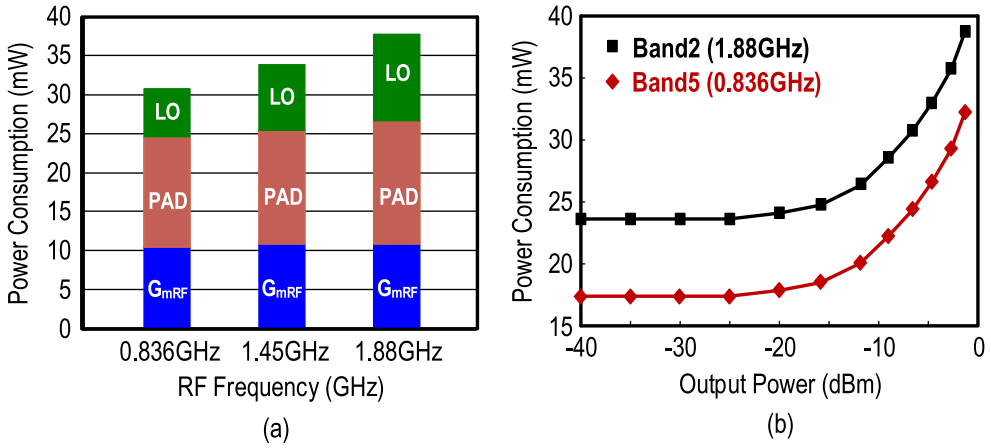

Fig. 20. TX mode. (a) Power breakdown at different RF. (b) Power consumption versus output power for the LTE Band2 and Band5.

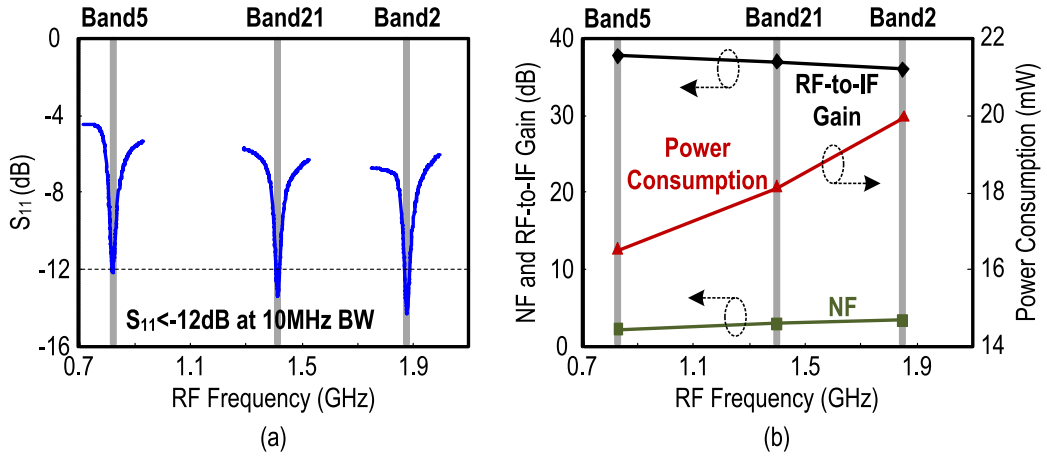

Fig. 21. RX-mode. (a) LO-defined narrowband S_{11}. (b) RF-to-IF gain, power consumption and NF.

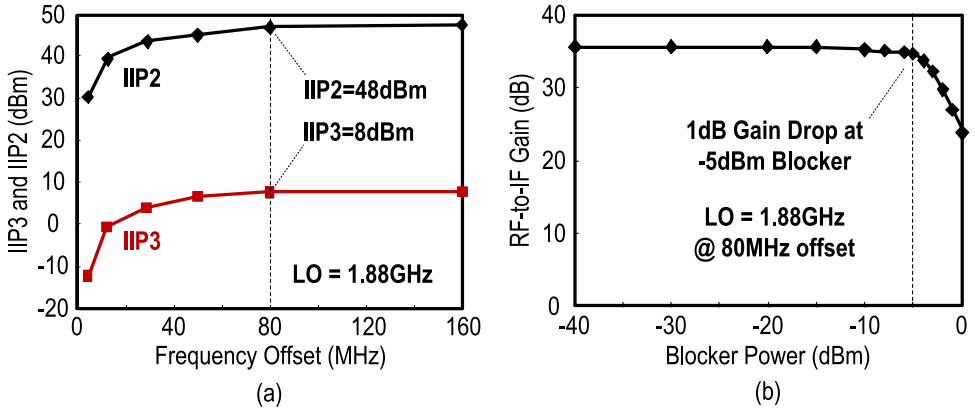

Fig. 22. RX-mode. (a) IIP2 and IIP3 profiles. (b) RF-to-IF gain versus blocker power at 80-MHz offset.

achieved with $S_{11} < -12$ dB and the position is simply defined by the LO. The unmatched OB parts are of low impedance favoring the blocker rejection. The NF is 2.2 dB and up to 3.2 dB at 1.88 GHz, as shown in Fig. 21(b). The NF goes up with frequency due to the BW limit of G_{mRF}. The total power consumption rises from 16.3 to 20 mW along with frequency mainly due to the LO generator, as shown in Fig. 21(b). G_{mRF} and the BB circuits consume 9.2 and 3.8 mW, respectively. The linearity is mainly assessed by IIP2, IIP3, and $P_{-1\mathrm{dB}}$ measurements. As shown in Fig. 22(a), the IB-IIP2/IIP3 is $+30/-12$ dBm, whereas the OB-IIP2/IIP3 is $+48/+8$ dBm at 80-MHz offset. Further, the IIP2 profile was measured by applying two-tone tests with frequency at $f_{\mathrm{LO}} + \Delta f$ and $f_{\mathrm{LO}} + \Delta f + 1$ MHz, whereas the IIP3 profile was obtained at $f_{\mathrm{LO}} + \Delta f$ and $f_{\mathrm{LO}} + 2\Delta f - 1$ MHz. At 80-MHz offset, the measured OB $P_{-1\mathrm{dB}}$ is -5 dBm [Fig. 22(b)].

The NF measured at BB is $\leq$3.2 dB at 5 MHz under LO = 0.836 and 1.88 GHz, as shown in Fig. 23(a). The blocker NF is

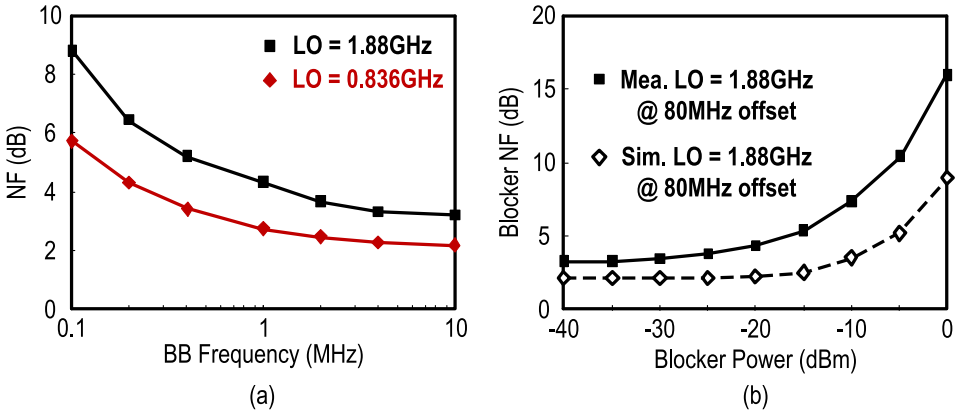

Fig. 23. RX-mode. (a) NF versus BB frequency. (b) Blocker NF at 80-MHz offset.

TABLE I
CHIP SUMMARY AND COMPARISON WITH THE STATE-OF-THE-ART MULTIBAND LTE TXs

	This Work - TX-Mode		JSSC'14 [8] [a]		ISSCC'15 [21]
TX Techniques	SC Gain Loop + Gain-Boosted N-Path Filter + Wideband Push-Pull PAD		Current-Mode + Class-A/B Power Mixer + Passive Baluns		Voltage-Mode Mixer + 33%-Duty-Cycle LO + Passive Baluns
On-chip Balun/Inductor	Zero		Four		Two
Multi-Band Flexibility	Defined by LO		Count on Baluns		Count on Baluns & Paths
External Matching Parts	Zero (compatible w/ RX)		Zero (only TX)		Zero (only TX)
	Measured Performances at different LTE Bands (LTE10 , 10MHz signal BW)				
	Band2 (1.88 GHz)	Band5 (0.836 GHz)	Band2 (1.88 GHz)	Band5 (0.836 GHz)	Band13 (0.782 GHz)
Output Power, P_{out} (dBm)	-1	-1.2	3.1	2.8	2
Output Noise (dBc/Hz) @ Freq. Offset (MHz)	-154.5 @ 80	-156 @ 45	-158 [b] @ 80	-159 [b] @ 45	-157.9 @ 31 (P_{out} = -1dBm)
$ACLR_{EUTRA1}$ (dBc)	-40.3	-41.6	-43	-43.4	-54
$ACLR_{EUTRA2}$ (dBc)	-51.9	-50.3	-54.5	-54.9	N/A
EVM (%)	2.0	2.1	1.4	1.4	0.8
Power (mW)	38.4	31.3	69.6 [c]	73.6 [c]	216
TX Efficiency (%)	2.1	2.4	2.9	2.6	0.7
Active Area (mm^2)	0.038		1.06 [c]		0.93
Supply Voltage (V)	1.1, 2.5		1.8		1.8
Technology	65 nm CMOS		55 nm LP CMOS		40 nm LP CMOS

[a] BBs are generated by on-chip DAC; [b] Measured with 50/20 Resource Block; [c] Without DAC, Biquad and 2 baluns

16 dB with a 0-dBm continuous-wave (CW) blocker injected at 80-MHz offset, as shown in Fig. 23(b). Estimated from simulations, 4 dB of such a blocker NF is due to the saturation of G_{mRF} and increase of the ON-resistance of SW_L; both lead to lower OB rejection. To improve it, the supply voltage and power budget of G_{mRF} should be enlarged. Another 5 dB is due to the gain compression at BB due to the use of a large R_{BR}. The reciprocal mixing of the LO phase noise contributes with additional 4 dB, and the remainder is mainly caused by the phase noise of the signal generator (Agilent E4438C) that provides the CW blocker signal. Moreover, the simulated blocker NF (<10 dB) from Cadence (qpss + qpnoise) is typically better than the measured, as the latter includes the collective effect of equipment's noise limit and uncertainty [22].

The performance summary is given in Table II and is compared with the state-of-the-art wideband RXs [6], [22], [23]. Similar NF and die size are achieved when comparing with [6], but here entailing only a single supply. Although this work consumes more power than [6], it operates at a 1.25× higher RF and has a 4.5× larger BB BW. The die area is at least 14× smaller than [22] and [23] at comparable power consumption, NF and OB-IIP3.

VII. CONCLUSION

An area-efficient SAW-less multiband TXR has been developed using an N-path SC gain loop, which can be reconfigured as a TX or RX by properly injecting and extracting the RF and BB signals. Specifically, with a four-path SC network as the feedback path of a gain stage, all essential TX and

TABLE II
CHIP SUMMARY AND COMPARISON WITH THE STATE-OF-THE-ART MULTIBAND RXS

	This Work – RX-Mode	ISSCC'15 [6]	JSSC'14 [22]	JSSC'14 [23]
RX Techniques	**Gain-Boosted-Mixer-First + N-Path Filtering + Switched-BB Extraction**	Gain-Boosted-Mixer-First + N-Path Filtering + Resistive-BB Extraction	Current-Reuse + Active/Passive N-Path Mixers	RF LNA + Passive Mixer + G_m-C + OpAmp
RF Input Style	Single-Ended	Single-Ended	Single-Ended	Differential
External Matching Parts	Zero	Zero	Zero	Transformer
Supply (V)	**1**	0.7, 1.2	1.2, 2.5	0.9
Power (mW) @ RF (GHz)	**20 @ 1.88**	11 @ 1.5	16.2 @ 0.85	40 @ 3
DSB NF [a] (dB)	**3.2 @ 1.88**	2.9 @ 1.5	5.5 @ 0.85	3.1 @ 3
BB BW (MHz)	**~9**	2	9	0.5 to 50
Die Size (mm^2)	**0.038 (include TX)**	0.028	0.55	~0.6
0-dBm Blocker NF (dB)	16 @ 80 MHz	13.5 @ 80 MHz	N/A	14 @ 80 MHz
OB-P_{1dB} (dBm)	-5 @ 80 MHz	-6 @ 80 MHz	-2.5 @ 50 MHz	-12.5 @ 80 MHz
OB-IIP3 (dBm)	+8	+13	+17.4	+3
OB-IIP2 (dBm)	+48	+50	+61	+80 (calibrated)
BB Filtering	1 Real Pole	1 Real Pole	2 Complex Poles + 2 Zeros	1 Real Pole + 1 Biquad
Voltage Gain (dB)	36	38	51 ± 1	70
Technology	65 nm CMOS	65 nm CMOS	65 nm CMOS	28 nm CMOS

[a] Measured flat NF at BB.

RX functions are embodied, i.e., signal amplification, high-Q bandpass filtering, and I/Q (de)modulation. The LO-defined bandpass filtering effectively suppresses the OB noise in the TX mode, and OB blockers in the RX mode. No on-chip inductors or external input-matching components are involved to cover a wide range of RF. The circuit analysis is based on an open-loop TX model using the Miller effect, which eases the calculation of the signal transfer function, and noise contributions of R_{BT}, G_{mRF} and ON-resistances of all switches. The RX mode features a switched BB-extraction technique to improve the RF. The very small area of the TXR renders it as an attractive candidate for cost reduction of SAW-less multiband cellular radios, though a higher TX output power (>0 dBm to account the PCB loss) and power-efficient variable gain control should be further developed for practical cell-phone applications.

REFERENCES

[1] L. E. Franks and I. W. Sandberg, "An alternative approach to the realization of network transfer functions: The *N*-path filter," *Bell Sys. Tech. J.*, vol. 39, no. 5, pp. 1321–1350, Sep. 1960.

[2] A. Ghaffari, E. A. M. Klumperink, M. C. M. Soer, and B. Nauta, "Tunable high-Q N-path band-pass filters: Modeling and verification," *IEEE J. Solid-State Circuits*, vol. 46, no. 5, pp. 998–1010, May 2011.

[3] A. Ghaffari, E. A. M. Klumperink, and B. Nauta, "Tunable N-path notch filters for blocker suppression: Modeling and verification," *IEEE J. Solid-State Circuits*, vol. 48, no. 6, pp. 1370–1382, Jun. 2013.

[4] C. Andrews and A. C. Molnar, "A passive mixer-first receiver with digitally controlled and widely tunable RF interface," *IEEE J. Solid-State Circuits*, vol. 45, no. 12, pp. 2696–2708, Dec. 2010.

[5] D. Murphy *et al.*, "A blocker-tolerant, noise-cancelling receiver suitable for wideband wireless applications," *IEEE J. Solid-State Circuits*, vol. 47, no. 12, pp. 2943–2963, Dec. 2012.

[6] Z. Lin, P.-I. Mak, and R. P. Martins, "A 0.028 mm^2 11 mW single-mixing blocker-tolerant receiver with double-RF N-path filtering, S_{11} centering, +13 dBm OB-IIP3 and 1.5-to-2.9dB NF," in *IEEE ISSCC Dig. Tech. Papers*, Feb. 2015, pp. 36–37.

[7] X. He and J. van Sinderen, "A low-power, SAW-less WCDMA transmitter using direct quadrature voltage modulation," *IEEE J. Solid-State Circuits*, vol. 44, no. 12, pp. 3448–3458, Dec. 2009.

[8] N. Codega, P. Rossi, A. Pirola, A. Liscidini, and R. Castello, "A current-mode, low out-of-band noise LTE transmitter with a class-A/B power mixer," *IEEE J. Solid-State Circuits*, vol. 49, no. 7, pp. 1627–1638, Jul. 2014.

[9] G. Qi, P.-I. Mak, and R. P. Martins, "A 0.038 mm^2 SAW-less multiband transceiver using an N-path SC gain loop," in *IEEE ISSCC Dig. Tech. Papers*, Feb. 2016, pp. 452–453.

[10] Z. Lin, P.-I. Mak, and R. P. Martins, "Analysis and modeling of a gain-boosted N-path switched-capacitor bandpass filter," *IEEE Trans. Circuits Syst. I, Reg. Papers*, vol. 61, no. 9, pp. 2560–2568, Sep. 2014.

[11] Z. Lin, P. I. Mak, and R. P. Martins, "A sub-GHz multi-ISM-band ZigBee receiver using function-reuse and gain-boosted N-path techniques for IoT applications," *IEEE J. Solid-State Circuits*, vol. 49, no. 12, pp. 2990–3004, Dec. 2014.

[12] A. Mirzaei, D. Murphy, and H. Darabi, "Analysis of direct-conversion IQ transmitters with 25% duty-cycle passive mixers," *IEEE Trans. Circuits Syst. I, Reg. Papers*, vol. 58, no. 10, pp. 2318–2331, Oct. 2011.

[13] A. Mirzaei and H. Darabi, "Analysis of imperfections on performance of 4-phase passive-mixer-based high-Q bandpass filters in SAW-less receivers," *IEEE Trans. Circuits Syst. I, Reg. Papers*, vol. 58, no. 5, pp. 879–892, May 2011.

[14] Kaelus Inc. *Report of EVM Degradation in LTE Systems by RF Filtering*, accessed on Apr. 1, 2017. [Online]. Available: http://www.kaelus.com/en

[15] M. Tohidian, I. Madadi, and R. B. Staszewski, "Analysis and design of a high-order discrete-time passive IIR low-pass filter," *IEEE J. Solid-State Circuits*, vol. 49, no. 11, pp. 2575–2587, Nov. 2014.

[16] Y. Xu, J. Zhu, and P. R. Kinget, "A blocker-tolerant RF front end with harmonic-rejecting N-path filtering," in *IEEE Radio Freq. Integr. Circuits Symp. Dig.*, Jun. 2014, pp. 39–42.

[17] *Anadigics LTE Power Amplifier*, accessed on Apr. 1, 2017. [Online]. Available: (AWT6652):http://www.anadigics.com/products/view/awt6652

[18] P.-I. Mak and R. P. Martins, "High-/mixed-voltage RF and analog CMOS circuits come of age," *IEEE Circuits Syst. Mag.*, vol. 1, no. 4, pp. 27–39, Dec. 2010.
[19] J. W. Park and B. Razavi, "Channel selection at RF using Miller bandpass filters," *IEEE J. Solid-State Circuits*, vol. 49, no. 12, pp. 3063–3078, Dec. 2014.
[20] L. Duipmans, R. E. Struiksma, E. A. M. Klumperink, B. Nauta, and F. E. V. Vliet, "Analysis of the signal transfer and folding in N-path filters with a series inductance," *IEEE Trans. Circuits Syst. I, Reg. Papers*, vol. 62, no. 1, pp. 263–272, Jan. 2015.
[21] Y.-H. Chen, N. Fong, B. Xu, and C. Wang, "An LTE SAW-less transmitter using 33% duty-cycle LO signals for harmonic suppression," in *IEEE ISSCC Dig. Tech. Papers*, Feb. 2015, pp. 172–173.
[22] F. Lin, P.-I. Mak, and R. P. Martins, "An RF-to-BB-current-reuse wideband receiver with parallel N-path active/passive mixers and a single-MOS pole-zero LPF," *IEEE J. Solid-State Circuits*, vol. 49, no. 11, pp. 2547–2559, Nov. 2014.
[23] B. van Liempd *et al.*, "A 0.9 V 0.4–6 GHz harmonic recombination SDR receiver in 28 nm CMOS with HR3/HR5 and IIP2 calibration," *IEEE J. Solid-State Circuits*, vol. 49, no. 8, pp. 1815–1826, Aug. 2014.

Gengzhen Qi (S'13) received the B.Sc. and M.Sc. degrees in electrical and electronics engineering, Faculty of Science and Technology, University of Macau, Macao, China, in 2011 and 2013, respectively, where he is currently pursuing the Ph.D. degree with the State-Key Laboratory of Analog and Mixed-Signal VLSI.

In 2016, has a 1-year internship position in the IMEC, Leuven, Belgium, where he was involved in RF tunable front-end module design in CMOS SOI technology. His current research interests include wideband-tunable CMOS RF transmitters, receivers, power amplifiers, and front-end techniques.

Pui-In Mak (S'00–M'08–SM'11) received the Ph.D. degree from the University of Macau (UM), Macao, China, in 2006.

He is currently an Associate Professor with the Department of Electrical and Computer Engineering, Faculty of Science and Technology, UM, where he is an Associate Director (Research) with the State-Key Laboratory of Analog and Mixed-Signal VLSI. His current research interests include analog and radio-frequency circuits and systems for wireless and biomedical and physical chemistry applications.

Dr. Mak was a technical program committee (TPC) Member of A-SSCC from 2013 to 2016. Since 2016, has been a TPC Member of the ISSCC and the ESSCIRC. He co-received numerous Merit Paper Awards: the ISSCC in 2016, the A-SSCC in 2015, the ASQED in 2013, the APCCAS in 2008, the DAC/ISSCC in 2005, the MWSCAS in 2004, the ASICON in 2003, the IEEE CASS Outstanding Young Author Award in 2010, the IEEE CASS Chapter-of-the-Year Award in 2009, and the Best Associate Editor of the IEEE TRANSACTIONS ON CIRCUITS AND SYSTEMS II from 2012 to 2013. He was an Editorial Board Member of the IEEE Press from 2014 to 2016; the Senior/Guest Editor of the IEEE JOURNAL ON EMERGING AND SELECTED TOPICS IN CIRCUITS AND SYSTEMS from 2014 to 2015, 2018; an Associate Editor of the IEEE TRANSACTIONS ON CIRCUITS AND SYSTEMS I from 2010 to 2011 and from 2014 to 2015, the IEEE TRANSACTIONS ON CIRCUITS AND SYSTEMS II from 2010 to 2013; the Guest Editor of the IEEE RFIC VIRTUAL JOURNAL in 2014 and the IEEE JOURNAL OF SOLID-STATE CIRCUITS in 2018; the Board-of-Governor of the IEEE Circuits and Systems Society from 2009 to 2011; and the Distinguished Lecturer of the IEEE Circuits and Systems Society from 2014 to 2015 and Solid-State Circuits Society from 2017 to 2018.

Rui P. Martins (M'88–SM'99–F'08) was born in 1957. He received the bachelor's, master's, and Ph.D. degrees, as well as the Habilitation for Full-Professor in electrical engineering and computers from the Department of Electrical and Computer Engineering, Instituto Superior Técnico (IST), Technical University (TU), Lisbon, Portugal, in 1980, 1985, 1992, and 2001, respectively.

From 1994 to 1997, he was the Dean of the Faculty, Faculty of Science and Technology, University of Macau (UM), Macau, China, where he has been with the Department of Electrical and Computer Engineering, since 1992, a Chair-Professor since 2013, and a Vice-Rector since 1997. Since 1980, he has been with the Department of Electrical and Computer Engineering, IST. From 2008, after the reform of the UM Charter, he was nominated after open international recruitment, and reappointed in 2013, as a Vice-Rector (Research) until 2018. Within the scope of his teaching and research activities he has taught 21 bachelor's and master's courses in UM, and has supervised (or co-supervised) 40 theses, Ph.D. (19) and master's (21). He was a Co-Founder of Chipidea Microelectronics (Macau) (now Synopsys) in 2001/2002, and created the Analog and Mixed-Signal VLSI Research Laboratory of UM, in 2003, elevated to State Key Laboratory of China (the first in Engineering in Macao), being its Founding Director, in 2011. He has co-authored six books and nine book chapters; 377 papers, in scientific journals (111), and in conference proceedings (266); as well as other 60 academic works, in a total of 470 publications; and holds 18 patents, U.S. (16) and Taiwan (2).

Dr. Martins received two government decorations: the Medal of Professional Merit from the Macao Government (Portuguese Administration) in 1999 and the Honorary Title of Value from the Macao SAR Government (Chinese Administration) in 2001. He was elected, unanimously, as a corresponding member of the Portuguese Academy of Sciences, Lisbon, being the only Portuguese Academician living in Asia, in 2010. He was the Founding Chairman of both the IEEE Macau Section during 2003–2005 and the IEEE Macau Joint-Chapter on Circuits and Systems (CAS)/Communications (COM) during 2005–2008 [2009 World Chapter of the Year of the IEEE CAS Society (CASS)]. He was the General Chair of the 2008 IEEE Asia-Pacific Conference on CAS—APCCAS'2008 and the ACM/IEEE Asia South Pacific Design Automation Conference—ASP-DAC'2016. He was the Vice-President for Region 10 (Asia, Australia, and the Pacific) of the IEEE CASS during 2009–2011, the Vice-President (World) Regional Activities and Membership of the IEEE CASS during 2012–2013, an Associate Editor of the IEEE TRANSACTIONS ON CAS (T-CAS) II: EXPRESS BRIEFS during 2010–2013, and the Best Associate Editor of T-CAS II from 2012 to 2013. He was a member of the IEEE CASS Fellow Evaluation Committee during 2013–2014 and CAS Society representative in the Nominating Committee, for the election in 2014, of the Division I (CASS/EDS/SSCS)—Director of the IEEE. He was a Nominations Committee Member in 2016 and is currently the Chair of the IEEE Fellow Evaluation Committee (class of 2018), both of the IEEE CASS.